letters to nature

the part of the production that takes place during autumn and winter (W_{Si} and W_C, which encompass 275 d). Thus, the annual production of Si and C are written:

$$P_{Si}^* = P_{Si} + W_{Si} \tag{3a}$$

$$P_C^* = P_N(C/N) + W_C \tag{3b}$$

In equation (3b), C/N = 62/11 (mol mol^{-1}) is the cellular elemental composition for this area[4]. The autumn–winter productivity is estimated from discrete measurements of Si and C production rates, using the ^{32}Si and ^{14}C isotopic technique, during the late winter ANTARES 3 cruise[13]. In the ice-free area, the productivity was 2.2 mmol Si m^{-2} d^{-1}, and 7.5 mmol C m^{-2} d^{-1}. Assuming constancy throughout winter and autumn in the ice-free area, this leads to a maximum of W_{Si} = 0.61 mol Si m^{-2} and W_C = 2.06 mol C m^{-2}. Note that these values are consistent, within ±15%, with model-derived estimates of winter and autumn production for the ice-free Indian sector of the Southern Ocean[15]. South of 58° S, that is, the northernmost limit of the ice extent during winter, W_{Si} and W_C were corrected using estimates of the seasonal ice-cover from the ERS1 satellite. For each month, we assume that the production is negligible when a station is totally covered by sea ice.

Combining Tables 1 and 2 shows that the spring–summer production represents from 70% (PFZ) to >90% (SIZ) of the annual biogenic silica production.

1. Boyle, E. A. J. Pumping iron makes thinner diatoms. *Nature* **393**, 733–734 (1998).
2. Nelson, D. M., Tréguer, P., Brzezinski, M. A., Leynaert, A. & Quéguiner, B. Production and dissolution of biogenic silica in the ocean: revised global estimates, comparison with regional data and relationship to biogenic sedimentation. *Glob. Biogeochem. Cycles* **9**, 359–372 (1995).
3. Tréguer, P. *et al.* The silica balance in the world ocean—a reestimate. *Science* **268**, 375–379 (1995).
4. Jennings, J. C. Jr, Gordon, L. I. & Nelson, D. M. Nutrient depletion indicates high primary productivity in the Weddell Sea. *Nature* **309**, 51–54 (1984).
5. Jacques, G. Is the concept of new-regenerated production valid for the Southern Ocean? *Mar. Chem.* **35**, 273–286 (1991).
6. Minas, H. J. & Minas, M. Net community production in "High Nutrient-Low Chlorophyll" waters of the tropical and Antarctic Ocean: grazing vs iron hypothesis. *Oceanol. Acta* **15**, 145–162 (1992).
7. Clowes, A. J. Phosphate and silicate in the Southern Ocean. *Discovery Rep.* **XIX**, 1–120 (1938).
8. Kamykowski, D. & Zentara, S. J. Circumpolar plant nutrient covariation in the Southern Ocean: pattern and processes. *Mar. Ecol. Prog. Ser.* **58**, 101–111 (1989).
9. Semeneh, M., Dehairs, F., Fiala, M., Elskens, M. & Goeyens, L. Seasonal variation of phytoplankton community structure and nitrogen uptake regime in the Indian sector of the Southern Ocean. *Polar Biol.* **20**, 259–272 (1998).
10. Davis, C. O. Continuous culture of marine diatoms under silicate limitation. II. Effect of light intensity on growth and nutrient uptake of *Skeletonema costatum*. *J. Phycol.* **12**, 291–300 (1976).
11. Takeda, S. Influence of iron availability on nutrient consumption ratio of diatoms in oceanic waters. *Nature* **393**, 774–777 (1998).
12. Quéguiner, B., Tréguer, P., Pecken, I. & Shareck, R. Biogeochemical dynamics and the silicon cycle in the Atlantic sector of the Southern Ocean during Austral spring 1992. *Deep-Sea Res.* **44**, 68–89 (1997).
13. Caubert, T. Couplage et découplage des cycles du carbone et du silicium dans le secteur Indien de l'Océan Austral. Thesis, Univ. Bretagne Occidentale (1998).
14. Wefer, G. & Fischer, G. Annual primary production and export flux in the Southern Ocean from sediment trap data. *Mar. Chem.* **35**, 597–613 (1991).
15. Pondaven, P., Ruiz-Pino, D., Druon, J. N., Fravalo, C. & Tréguer, P. Factors controlling silicon and nitrogen biogeochemical cycles in high nutrient, low chlorophyll systems (the Southern Ocean and the North Pacific – Comparison with a mesotrophic system (the North Atlantic). *Deep-Sea Res.* **46**, 1923–1968 (1999).
16. Arrigo, K., Worthon, D., Schnell, A. & Lizotte, M. P. Primary production in Southern Ocean waters. *J. Geophys. Res.* **103**, 15587–15600 (1998).
17. Blain, S., Leynaert, A., Tréguer, P., Chrétiennot-Dinet, M.-J. & Rodier, M. Biomass, growth rates and limitation of equatorial Pacific diatoms. *Deep-Sea Res.* **44**, 1255–1275 (1997).
18. Nelson, D. M. & Brzezinski, M. A. Diatom growth and productivity in an oligotrophic midocean gyre: a 3-yr record from the Sargasso Sea near Bermuda. *Limnol. Oceanogr.* **42**, 473–486 (1997).
19. Lampitt, R. & Antia, A. N. Particle flux in deep-seas: regional characteristics and temporal variability. *Deep-Sea Res.* **44**, 1377–1403 (1997).
20. Honjo, S., Dymond, J., Collier, R. & Manganini, S. J. Export production of particles to the interior of the Equatorial Pacific Ocean during the 1992 EqPac experiment. *Deep-Sea Res.* **42**, 831–870 (1995).
21. Deuser, W. G., Jickells, T. D., King, P. & Commeau, J. A. Decadal and annual changes in biogenic opal and carbonate fluxes to the deep Sargasso Sea. *Deep-Sea Res.* **33**, 225–246 (1995).
22. Berger, W. H. & Wefer, G. Export production: seasonality and intermittency, and paleoceanographic implications. *Paleoceanogr. Paleoclimatol. Paleoecol.* **89**, 245–254 (1990).
23. Bacon, M. P. Glacial to Interglacial changes in carbonate and clay sedimentation in the Atlantic ocean estimated from ^{230}Th measurements. *Isotope Geosci.* **2**, 97–111 (1984).
24. Francois, R., Bacon, M. P., Altabet, M. A. & Labeyrie, L. D. Glacial/interglacial changes in sediment rain rate in the SW Indian sector of Subantarctic waters as recorded by ^{230}Th, ^{231}Pa, U, and ^{15}N. *Paleoceanography* **8**, 611–629 (1993).
25. Rabouille, C., Gaillard, J. F., Tréguer, P. & Vincendeau, M. A. Biogenic silica recycling in surficial sediments across the Polar Front of the Southern Ocean (Indian Sector). *Deep-Sea Res.* **44**, 1151–1176 (1997).
26. Berelson, W. M. *et al.* Biogenic budgets of particle rain, benthic remineralization and sediment accumulation in the Equatorial Pacific. *Deep-Sea Res.* **44**, 2251–2282 (1997).
27. Sayles, F. L. *et al.* The benthic cycle of biogenic opal at the Bermuda Atlantic Time series site. *Deep-Sea Res.* **43**, 383–409 (1996).
28. Gordon, A. L., Chen, C. T. A. & Metcalf, W. G. Winter layer entrainment of the Weddell Deep Water. *J. Geophys. Res.* **89**, 637–640 (1984).
29. Tréguer, P., Kamatami, A., Gueneley, S. & Quéguiner, B. Kinetics of dissolution of Antarctic diatoms frustules and the biogeochemical cycle of silicon in the Southern Ocean. *Polar Biol.* **9**, 397–403 (1989).
30. Bianchi, M., Feliatra, F., Tréguer, P., Vincendeau, M. & Morvan, J. Nitrification rates, ammonium and nitrate distribution in upper layers of the water column and in the sediments of the Indian sector of the Southern Ocean. *Deep-Sea Res.* **44**, 1017–1032 (1997).

Constraints on the composition of the Earth's core from *ab initio* calculations

D. Alfè*, M. J. Gillan† & G. D. Price*

* *Research School of Geological and Geophysical Sciences, Birkbeck College and University College London, Gower Street, London WC1E 6BT, UK*
† *Physics and Astronomy Department, University College London, Gower Street, London WC1E 6BT, UK*

Knowledge of the composition of the Earth's core[1–3] is important for understanding its melting point and therefore the temperature at the inner-core boundary and the temperature profile of the core and mantle. In addition, the partitioning of light elements between solid and liquid, as the outer core freezes at the inner-core boundary, is believed to drive compositional convection[4], which in turn generates the Earth's magnetic field. It is generally accepted that the liquid outer core and the solid inner core consist mainly of iron[1]. The outer core, however, is also thought to contain a significant fraction of light elements, because its density—as deduced from seismological data and other measurements—is 6–10 per cent less than that estimated for pure liquid iron[1–3]. Similar evidence indicates a smaller but still appreciable fraction of light elements in the inner core[5,6]. The leading candidates for the light elements present in the core are sulphur, oxygen and silicon[3]. Here we obtain a constraint on core composition derived from *ab initio* calculation of the chemical potentials of light elements dissolved in solid and liquid iron. We present results for the case of sulphur, which provide strong evidence against the proposal that the outer core is close to being a binary iron–sulphur mixture[7].

Our proposed constraint is simply stated. If, as commonly assumed, the solid and liquid are in thermodynamic equilibrium at the inner-core boundary (ICB), the chemical potentials of a given element in both phases must be equal at the boundary. This condition determines the ratio of concentrations of elements in the solid and the liquid phase, and hence the relation between the outer-core and inner-core densities, which must agree with seismic measurements of these densities.

The chemical potential μ_X of a solute X in a solid or liquid solution is conventionally expressed as $\mu_X = \mu_X^\dagger + k_B T \ln a_X$, where $\mu_X^\dagger$ is a constant and a_X is the activity[8]. To reflect the fact that a_X becomes equal to the mole fraction c_X in the dilute limit $c_X \rightarrow 0$, it is common practice to write $a_X = \gamma_X c_X$, where the activity coefficient, γ_X, has the property $\gamma_X \rightarrow 1$ as $c_X \rightarrow 0$ (ref. 8). Here we rearrange the expression for μ_X as $\mu_X = \tilde{\mu}_X + k_B T \ln c_X$, where $\tilde{\mu}_X$ is defined to be equal to $\mu_X^\dagger + k_B T \ln \gamma_X$. Equality of the chemical potentials μ_X^l and

$\tilde{\mu}_X^s$ in coexisting liquid and solid (superscripts l and s respectively) then requires that

$$\tilde{\mu}_X^l + k_B T \ln c_X^l = \tilde{\mu}_X^s + k_B T \ln c_X^s \qquad (1)$$

or equivalently

$$c_X^s / c_X^l = \exp[(\tilde{\mu}_X^l - \tilde{\mu}_X^s)/k_B T] \qquad (2)$$

This means that the ratio of the mole fractions c_X^s and c_X^l of X in the solid and liquid solution is determined by the liquid and solid thermodynamic quantities $\tilde{\mu}_X^l$ and $\tilde{\mu}_X^s$. Although liquid–solid equilibrium in the iron–sulphur (Fe–S) system has been experimentally studied up to pressures of around 60 GPa (ref. 9), there seems little immediate prospect of obtaining experimental data for $\tilde{\mu}_X^l - \tilde{\mu}_X^s$ for Fe–S or any other binary Fe–X system at the much higher ICB pressure of 330 GPa. However, we will show here that a fully *ab initio* calculation of $\tilde{\mu}_X^l$ and $\tilde{\mu}_X^s$ is achievable for S.

If we can obtain accurate values of $\tilde{\mu}_X^l$ and $\tilde{\mu}_X^s$, then we can test any binary alloy (Fe–X) model for the core as follows: (1) we use *ab initio* calculations on the iron alloy liquid at the ICB pressure to determine the liquid mole fraction c_X^l needed to reproduce the measured ICB density of the outer core; (2) we use equation (2) to determine c_X^s; (3) we use *ab initio* calculations on the Fe–X solid with this c_X^s value to deduce its density at the ICB pressure. If this approach disagrees with the density deduced from seismic measurements[10] the model can be ruled out. (Allowance must, of course, be made for uncertainties in both seismic and *ab initio* values.)

The use of *ab initio* molecular dynamics based on density-functional theory (DFT) to investigate liquid Fe–X alloys under Earth's core conditions, and in particular to determine the impurity mole fractions needed to account for a specified density reduction, has been described elsewhere. In our earlier work on liquid Fe–S (refs 11, 12), we showed that at ICB pressures an S mole fraction of $c_S^l = 18.75\%$ reduces the density from that of pure Fe by 8%. In fact, our most recent calculations[13] show that the density of pure liquid Fe at ICB conditions is ~6% higher than the seismic density, so that the required mole fraction of S is estimated to be equal to 15%. This is close to estimates in the region of 16% deduced from experimental equation-of-state measurements[14].

The techniques developed here for calculating chemical potentials build on recent progress in *ab initio* calculations of free energies[15–18]. We start from the basic definition that μ_X (per atom) can either represent the change of Gibbs free energy when an atom of X is added to the system at constant temperature T and pressure P, or the change of Helmholtz free energy F at constant T and volume V. Computationally, it is convenient to work with the difference $\mu_X - \mu_{Fe}$ of chemical potentials of X and Fe, which represents the change of free energy when an atom of Fe is replaced by an atom of X. The chemical potential μ_X and hence $\tilde{\mu}_X$ is obtained from $\mu_X - \mu_{Fe}$ by making use of the Gibbs free energies of pure solid and liquid Fe calculated in our recent work[16]. (In the following, where necessary, we shall use the quantity $\tilde{\mu}_{Fe}$ defined in the analogous way to $\tilde{\mu}_X$ by the equation $\mu_{Fe} = \tilde{\mu}_{Fe} + k_B T \ln c_{Fe}$, where $c_{Fe} = 1 - c_X$ represents the mole fraction of Fe.)

For the crystal, the change of F associated with formation of a substitutional X impurity by replacement of an Fe atom by an X atom is readily computed in the limit $c_X \rightarrow 0$. (For S, O and Si impurities, interstitial formation is expected to be energetically very unfavourable, and can be ignored.) In the expression $F - E - TS$, the change of internal energy E is the difference between the *ab initio* energy of the perfect Fe crystal and that of the same crystal with a single substitutional X atom. The contribution from the change of entropy S can be expressed in the harmonic approximation as $-k_B T \Sigma_n [\ln(\hbar \omega_n' / k_B T) - \ln(\hbar \omega_n / k_B T)]$, where ω_n and ω_n' are the lattice vibrational frequencies of the Fe crystal without and with the X atom. The *ab initio* calculation of lattice vibrational frequencies is well-established, and presents no major problems[19]. Here we use our

implementation of the small-displacement method[17,20] to calculate all the ω_n and ω_n' in a large supercell of crystal. We will return below to the estimation of anharmonic corrections.

To calculate μ_X^s away from the dilute limit, we note that the part of the statistical mechanics associated with the rearrangement of X atoms on lattice sites is rigorously equivalent to a lattice-gas problem, for which we can use standard Monte Carlo methods[21] to evaluate the free energy. The crucial input from *ab initio* calculations is the interaction free energy of X atoms when they are on neighbouring sites. This interaction free energy is just the change in F when a pair of X atoms, initially on distant sites, are placed on nearest-neighbour sites. The change in E in this process is obtained from a straightforward *ab initio* calculation, and the contribution from the entropy change is also obtained from an *ab initio* calculation of the lattice vibrational frequencies for the X–X pair on neighbouring sites.

For liquid Fe–X, we calculated the difference $\mu_X - \mu_{Fe}$ using "thermodynamic integration"[22]. This is a general technique for computing the Helmholtz free energy difference $F_1 - F_0$ of two systems containing the same number N of atoms, but having different total energy functions $U_1(\mathbf{r}_1, \dots \mathbf{r}_N)$ and $U_0(\mathbf{r}_1, \dots \mathbf{r}_N)$, where $\mathbf{r}_i$ is the position of atom i. The difference $F_1 - F_0$ represents the reversible work done when continuously switching the total energy function from U_0 to U_1 at constant volume, and can be expressed as

$$F_1 - F_0 = \int_0^1 d\lambda \langle U_1 - U_0 \rangle_\lambda \qquad (3)$$

where the average $\langle \dots \rangle$ is calculated in thermal equilibrium for the system governed by the 'hybrid' energy function $U_\lambda = (1 - \lambda)U_0 + \lambda U_1$. This well-established *ab initio* calculation technique of liquid-state free energies[15,23] was used in our recent investigation[16] of the high-pressure melting curve of Fe. In order to compute $\mu_X - \mu_{Fe}$, we let U_0 be the total energy for the system with N_{Fe} atoms of Fe and N_X of X, and we let U_1 be the same for $N_{Fe} - 1$ atoms of Fe and $N_X + 1$ of X. We evaluate $\langle U_1 - U_0 \rangle_\lambda$ by performing *ab initio* molecular dynamics with time evolution generated by U_λ, and taking the time average of $U_1 - U_0$. We repeat this procedure for several values of λ, and the integration over λ is done numerically.

This type of 'transmutation' of Fe into S obviously does not correspond to a real-world process, but in terms of *ab initio* statistical mechanics is a perfectly rigorous way of obtaining the chemical potential difference $\tilde{\mu}_X - \tilde{\mu}_{Fe}$. It demands an unusual kind of simulation: for the atom positions $\mathbf{r}_1, \dots \mathbf{r}_N$ at each instant of time, we have to perform two independent *ab initio* calculations, one for each chemical composition. As well as U_0 and U_1 for the given positions, we calculate two sets of *ab initio* forces $\mathbf{F}_{0i} = -\nabla_i U_0$ and $\mathbf{F}_{1i} = -\nabla_i U_1$, and the linear combinations $\mathbf{F}_{\lambda i} = (1 - \lambda)\mathbf{F}_{0i} + \lambda \mathbf{F}_{1i}$ are used to generate the time evolution. In practice, the statistical accuracy is rather poor if one 'transmutes' only a single Fe atom into X, and it is preferable to 'transmute' several atoms at the same time. Instead of $\tilde{\mu}_X - \tilde{\mu}_{Fe}$ for a given mole fraction c_X, this then yields an integral of $\mu_X - \mu_{Fe}$ over a range of c_X values. The results obtained by 'transmuting' different numbers of atoms can then be processed to obtain $\tilde{\mu}_X - \tilde{\mu}_{Fe}$ as a function of c_X. Once we obtain $\tilde{\mu}_X - \tilde{\mu}_{Fe}$ for both solid and liquid, the difference $\tilde{\mu}_X^l - \tilde{\mu}_X^s$ which determines c_X^s / c_X^l is obtained by using values for μ_{Fe} in pure Fe obtained in our earlier *ab initio* calculations[16].

Our practical *ab initio* calculations on the binary Fe–S system employed exactly the same DFT techniques with plane-wave basis sets and ultrasoft pseudopotentials described in detail in our earlier work on the high-pressure Fe–S and Fe–O liquids[11,12]. The calculations were done using the software package VASP[24], which is exceptionally efficient and stable for metallic systems. We have already reported extensive comparisons with a range of experimental data and with other implementations of DFT which demon-

strate the accuracy and reliability of the techniques[13]. We focus mainly on results for the S chemical potentials obtained at the thermodynamic state $P = 370$ GPa and $T = 7{,}000$ K, which is close to the ICB pressure but at a somewhat higher temperature; results obtained at $P = 80$ GPa and $T = 3{,}500$ K are mentioned later. Our solid phase is taken to have the hexagonal-close-packed (h.c.p.) structure, because the available evidence indicates that this is the stable structure for Fe under inner-core conditions[25].

In the high-P/high-T state, we find the dilute-limit value $\mu_S^{\dagger l} - \mu_S^{\dagger s} = -0.25$ eV. As expected, its negative values favours partitioning of S into the liquid, but its magnitude is smaller than $k_B T$, so that the partitioning is weak: if we put this value into equation (2), we obtain $c_S^s/c_S^l = 0.66$. Even more importantly, we find that the variation of activity coefficients (γ_S) with concentration cannot be ignored, and that both $\tilde{\mu}_S^l$ and $\tilde{\mu}_S^s$ increase strongly with increasing mole fraction of S. For concentrations up to ~20%, $\tilde{\mu}_S$ is well represented as $\tilde{\mu}_S = \mu_S^{\dagger} + \lambda_S c_S$, with respective liquid and solid values of λ_S of 6.3 and 6.1 eV. Equation (2) shows that the similarity of these λ_S values will prevent the solid and liquid concentrations differing significantly. For a value of $c_S^l = 0.15$, we find the solution $c_S^s = 0.13$. The conclusion is that if the outer core is a binary Fe–S mixture, the mole fraction of S in the inner core will be ~13%.

This is completely incompatible with seismic measurements, which give an accurate value for the density difference between liquid and solid at the ICB equal to 4.5 ± 0.5% (ref. 10). According to our earlier *ab initio* calculations[16], incompatibility arises due to a density difference between coexisting liquid and solid pure Fe at the ICB pressure of only 1.6%. Our present calculations show that the S atomic volume in both solid and liquid is almost identical to that of Fe. To a sufficient accuracy it is true that the fractional change of density in each phase can be calculated simply as $c_S(m_S - m_{Fe})/m_{Fe}$, where m_S and m_{Fe} are the atomic masses of S and Fe. This means that if c_S^l and c_S^s were equal, the density difference between liquid and solid would remain unchanged at 1.6%. The small difference between c_S^l and c_S^s has the effect of increasing the density difference only to 2.5%, which is still well below the seismic value of 4.5 ± 0.5%. We therefore rule out the binary Fe–S model for core composition. Even without density data, we observe that the very high solubility of S in the solid can cause another major problem. It is generally believed that convection in the outer core is driven by the partitioning of light impurities into the liquid, which is also incompatible with the very weak partitioning found here.

If our *ab initio* techniques are reliable, they must yield predictions that are compatible with the known Fe–S phase diagram at low pressures and temperatures. Measurements[26] show that Fe–S is a normal eutectic system at ambient pressure, with a strong depression of freezing point, and almost complete partitioning of S into the liquid phase on the Fe-rich side of the phase diagram. Our *ab initio* results at $P = 80$ GPa and $T = 3{,}500$ K give the dilute-limit value $\mu_S^{\dagger l} - \mu_S^{\dagger s} = -0.36$ eV, which is significantly less than our high-P/high-T value. We also find that the variation of activity coefficients γ_S with concentration is much weaker, with λ_S values equal to 1.4 and 2.4 in the liquid and solid, respectively. At temperatures equal to and below the ambient-pressure melting temperature of Fe (1,810 K), we therefore predict strong partitioning of S to the liquid phase, as expected from the phase diagram.

Although the consequences of our calculated chemical potentials are striking, their values are not. As stressed above, S and Fe atoms are almost exactly the same size. The (free) energetic effects of replacing Fe by S should therefore be almost identical in both phases. Near the Fe melting curve, a difference $\tilde{\mu}_S^l - \tilde{\mu}_S^s$ of more than a few tenths of an eV would therefore have been surprising. The cause of the strong increase of $\tilde{\mu}_S$ with concentration is also very clear. We showed earlier that there is an effective repulsion between S atoms in the high-pressure liquid phase[11]. This arises because the S valence states lie at least 10 eV below the Fermi energy, so that

chemical bonding between S atoms is very weak. If two isolated S atoms are brought together, two Fe–S bonds are lost and one Fe–Fe bond is gained. The relative strengths of the Fe–S and Fe–Fe bonds mean that this process is energetically unfavourable. We also note that Boehler's measurements[9] on eutectic behaviour in the Fe–S system up to pressures of ~60 GPa indicate that increasing pressure reduces the depression of the freezing point. These measurements were interpreted by suggesting that "Fe and FeS exhibit binary solid-solution behaviour rather than eutectic behaviour at core pressures"[9], which is exactly what our present calculations show.

Are the *ab initio* calculations precise enough to support our claim that the binary Fe–S model fo the core is untenable? We stress that high precision is both expected and unnecessary. DFT calculations are at their best when atoms change neither the electronic structure nor their environment. As the close-packed structures of the solid and liquid are almost identical at ICB pressures, high precision is expected[13]. The obvious omission in our calculations is to neglect anharmonicity in the solid. In our recent calculations of the free energy of h.c.p. Fe under Earth's core conditions[16,17], we have shown that the anharmonic contribution to the free energy can be ~60 meV per atom on the melting curve, so the error in our values for $\tilde{\mu}_S^l - \tilde{\mu}_S^s$ might be as large as this. But even in the unlikely event that the chemical potential differences varied by several tenths of an eV, our conclusions would not change, as the effective repulsion between S atoms forces near-equalization of the solid and liquid concentrations.

Even if one adopts an extremely cautious view of the precision achievable by present *ab initio* calculations, we believe that technical developments now underway will answer all doubts on this score. Quantum Monte Carlo (QMC) techniques[27] have been demonstrated to give considerably higher precision for energetics than the best DFT calculations[28], and QMC calculations on condensed-matter systems of well over 100 atoms have recently been reported[29]. The use of QMC in the near future to tackle systems as challenging as liquid Fe–X alloys is not unthinkable.

The main conclusion of this work is that a simple binary Fe–S core composition is incompatible with the geophysical facts. But the general constraint provided by *ab initio* chemical potentials should be capable of telling us much more than just this. For example, if we take a ternary model, such as Fe–S–O or Fe–S–Si, the constraint should uniquely fix the two impurity concentrations. Recent experiments[30] suggest that Si dissolves in liquid Fe only under strongly reducing conditions, so that the four-component model Fe–S–Si–O probably need not be considered. This suggests that *ab initio* constraints may ultimately turn the problem of core composition from being completely insoluble to being at least partially soluble. □

1. Birch, F. Density and composition of mantle and core. *J. Geophys. Res.* **69**, 4377–4388 (1964).
2. Ringwood, A. E. Composition of the core and implications for the origin of the Earth. *Geochem. J.* **11**, 111–135 (1977).
3. Poirier, J. P. Light elements in the Earth's outer core: a critical review. *Phys. Earth Planet. Inter.* **85**, 319–337 (1994).
4. Loper, D E. The gravitationally powered dynamo. *Geophys. J. R. Astron. Soc.* **54**, 389–404 (1978).
5. Jephcoat, A. & Olson, P. Is the inner core of the Earth pure iron? *Nature* **325**, 332–335 (1987).
6. Stixrude, L., Wasserman, E. & Cohen, R. E. Composition and temperature of the Earth's inner core. *J. Geophys. Res.* **102**, 24729–24739 (1997).
7. Rama Murthy, V. & Hall, H. T. The chemical composition of the Earth's core: possibility of sulfur in the core. *Phys. Earth Planet. Inter.* **2**, 276–282 (1970).
8. Atkins, P. W. *Physical Chemistry* Ch. 7 (Oxford University Press, 1994).
9. Boehler, R. Fe-FeS eutectic temperatures to 620 kbar. *Phys. Earth Planet. Inter.* **96**, 181–186 (1996).
10. Masters, T. G. & Shearer, P. M. Summary of seismological constraints on the structure of the earth's core. *J. Geophys. Res.* **95**, 21691–21695 (1990).
11. Alfè, D. & Gillan, M. J. First-principles simulation of liquid Fe-S under Earth's core conditions. *Phys. Rev. B* **58**, 8248–8256 (1990).
12. Alfè, D., Price, G. D. & Gillan, M. J. Oxygen in the Earth's core: A first-principles study. *Phys. Earth Planet. Inter.* **110**, 191–210 (1999).
13. Alfè, D., Kresse, G. & Gillan, M. J. Structure and dynamics of liquid iron under Earth's core conditions. *Phys. Rev. B* **61**, 132–142 (2000).
14. Ahrens, T. J. Equations of state of iron sulfide and constraints on the sulfur content of the Earth. *J. Geophys. Res.* **84**, 985–998 (1979).

15. de Wijs, G. A., Kresse, G. & Gillan, M. J. First-order phase transitions by first-principles free-energy calculations: The melting of Al. *Phys. Rev. B* **57**, 8223–8334 (1998).

16. Alfè, D., Gillan, M. J. & Price, G. D. The melting curve of iron at the pressures of the Earth's core from *ab initio* calculations. *Nature* **401**, 462–464 (1999).

17. Alfè, D., Gillan, M. J. & Price, G. D. Thermodynamics of hexagonal-close-packed iron under Earth's core conditions. *Phys. Rev. B* (submitted).

18. Alfè, D., de Wijs, G. A., Kresse, G. & Gillan, M. J. Recent developments in ab-initio thermodynamics. *Int. J. Quant. Chem.* **77**, 871–879 (2000).

19. Giannozzi, P., de Gironcoli, S., Pavone, P. & Baroni, S. *Ab initio* calculations of phonon dispersions in semiconductors. *Phys. Rev. B* **43**, 7231–7242 (1991).

20. Kresse, G., Furthmüller, J. & Hafner, J. *Ab initio* force-constant approach to phonon dispersion relations of diamond and graphite. *Europhys. Lett.* **32**, 729–734 (1995).

21. Chandler, D. *Introduction to Modern Statistical Mechanics* (Oxford University Press, 1987).

22. Frenkel, D. & Smit, B. *Understanding Molecular Simulation* Ch. 4 (Academic, New York, 1987).

23. Sugino, O. & Car, R. *Ab initio* molecular dynamics study of first-order phase transitions: melting of silicon. *Phys. Rev. Lett.* **74**, 1823–1826 (1995).

24. Kresse, G. & Furthmüller, J. Efficient iterative schemes for *ab initio* total-energy calculations using a plane-wave basis set. *Phys. Rev. B* **54**, 11169–11186 (1996).

25. Vočadlo, L., Brodholt, J., Alfè, D., Price, G. D. & Gillan, M. J. The structure of iron under the conditions of the Earth's inner core. *Geophys. Res. Lett.* **26**, 1231–1234 (1999).

26. Usselman, T. M. Experimental approach to the state of the core: part I. The liquidus relations of the Fe-rich portion of the Fe-Ni-S system from 30 to 100 kb. *Am. J. Sci.* **275**, 278–290 (1975).

27. Hammond, B. L., Lester, W. A. Jr & Reynolds, P. J. *Monte Carlo Methods in Ab Initio Quantum Chemistry* (World Scientific, Singapore, 1994).

28. Rajagopal, G., Needs, R. J., James, A., Kenny, S. D. & Foulkes, W. M. C. Variational and diffusion quantum Monte Carlo calculations at nonzero wave vectors: Theory and applications to diamond-structure germanium. *Phys. Rev. B* **51**, 10591–10600 (1995).

29. Kent, P. R. C. *et al.* Finite-size errors in quantum many-body simulations of extended systems. *Phys. Rev. B* **59**, 1917–1929 (1999).

30. Kilburn, M. R. & Wood, B. J. Metal-silicate partitioning and the incompatibility of S and Si during core formation. *Earth Planet. Sci. Lett.* **152**, 139–148 (1997).

....

Detection and classification of atmospheric methane oxidizing bacteria in soil

Ian D. Bull*, **Nisha R. Parekh**†, **Grahame H. Hall**‡, **Philip Ineson**§ & **Richard P. Evershed***

* *School of Chemistry, University of Bristol, Cantock's Close, Bristol BS8 1TS, UK*
† *Institute of Terrestrial Ecology, Merlewood Research Station, Grange-over-Sands, Cumbria LA11 6JU, UK*
‡ *Institute of Freshwater Ecology, Far Sawrey, Ambleside, Cumbria LA22 0LP, UK*
§ *Department of Biology, University of York, P.O. Box 373, York YO10 5YW, UK*

....

Well-drained non-agricultural soils mediate the oxidation of methane directly from the atmosphere, contributing 5 to 10% towards the global methane sink[1,2]. Studies of methane oxidation kinetics in soil infer the activity of two methanotrophic populations: one that is only active at high methane concentrations (low affinity) and another that tolerates atmospheric levels of methane (high affinity). The activity of the latter has not been demonstrated by cultured laboratory strains of methanotrophs, leaving the microbiology of methane oxidation at atmospheric concentrations unclear[3,4]. Here we describe a new pulse-chase experiment using long-term enrichment with $^{12}CH_4$ followed by short-term exposure to $^{13}CH_4$ to isotopically label methanotrophs in a soil from a temperate forest. Analysis of labelled phospholipid fatty acids (PLFAs) provided unambiguous evidence of methane assimilation at true atmospheric concentrations (1.8–3.6 p.p.m.v.). High proportions of ^{13}C-labelled C_{18} fatty acids and

the co-occurrence of a labelled, branched C_{17} fatty acid indicated that a new methanotroph, similar at the PLFA level to known type II methanotrophs, was the predominant soil micro-organism responsible for atmospheric methane oxidation.

Culturable methane oxidizing bacteria are classified into types I, II and X depending on the guanine and cytosine content of their DNA, intracellular membrane arrangement, carbon assimilation pathway and PLFA composition[3]. Active soil microbial populations utilizing a ^{13}C-labelled substrate will readily incorporate ^{13}C into membrane lipid components such as PLFAs. Recent work has demonstrated the power of ^{13}C-labelling to link lipid biomarkers to other biogeochemical processes in lake and marine sediments[5,6]. We have applied similar techniques to a soil to investigate the oxidation of methane at atmospheric concentrations.

Soils used for pulse-chase labelling were obtained from a Sitka Spruce plantation in North Wales, UK. Mull-board ploughing before tree planting in 1959 produced a repeating microtopographic pattern consisting of a plough furrow and ridge followed by an undisturbed ridge. The plough ridges have an inversion of the original stratification of soil horizons resulting in a buried organic horizon beneath an overturned mineral horizon; soil cores from these ridges exhibited high rates of atmospheric methane consumption (mean rate is 77 μg m^{-2} h^{-1}, standard error (s.e.) = 2, $n = 7$). Laboratory experiments at atmospheric and elevated concentrations demonstrated that soils from both the buried organic and mineral horizons showed similar kinetics of oxidation, but activities were generally lower in the mineral soil. Increasing the initial concentration of methane from 1.8 to 300 parts per million by volume (p.p.m.v.) for both soils showed typical Michaelis–Menten kinetics with K_m methane concentration at half of the maximal reaction rate values of 25 and 56 p.p.m.v. for the buried organic and mineral soils, respectively (Fig. 1). Rapid rates of methane consumption, characteristic of high-affinity methane-oxidation kinetics, were observed in both soils below 50 p.p.m.v. methane. Concentrations of methane, which induce oxidation kinetics indicative of high (1.8–3.6 p.p.m.v.) and low (100 p.p.m.v.) affinity methanotroph populations, were chosen for the ^{13}C pulse-chase experiment in soil columns.

The distribution of PLFAs shown in Fig. 2 (for the buried organic horizon) is typical of all the soil samples analysed; the only significant difference between the two soil types is the lower overall abundance of PLFAs in the mineral soil ($\sim$35 μg g$^{-1}_{TOC}$); where TOC refers to 'total organic carbon' compared with the buried organic
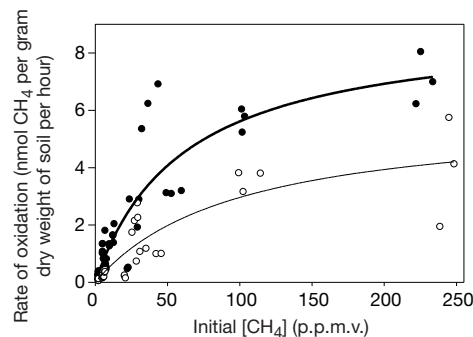

Figure 1 Rates of methane oxidation between 1.5 and 250 p.p.m.v. by forest soil from the mineral and buried organic layers. Lines represent direct nonlinear regression analysis and show typical Michaelis–Menten kinetics. Data points show the mineral layer (white circles) and buried organic layer (black circles). Application of the Lineweaver Burke plot provided a significant regression ($P < 0.001$) for both data sets that were used to calculate the apparent K_m (methane concentration at half of the maximal reaction rate) and V_{max} (maximal reaction rate) values for each soil. Regression for mineral soil $R^2 = 0.78$, apparent $K_m = 56$ p.p.m.v., apparent $V_{max} = 2.8$ nmol per gram dry weight of soil per hour. Regression for organic soil $R^2 = 0.82$, apparent $K_m = 25$ p.p.m.v., apparent $V_{max} = 3.7$ nmol per gram dry weight of soil per hour.

175